Bioactive Materials 5 (2020) 1044–1052

Contents lists available at ScienceDirect

Bioactive Materials

journal homepage: http://www.keaipublishing.com/biomat

Insight into vitronectin structural evolution on material surface chemistries: The mediation for cell adhesion

Tianjie Li[a,b], Lijing Hao[a,b], Jiangyu Li[d], Chang Du[a,b,c,e,*], Yingjun Wang[a,b,c,**]

[a] Department of Biomedical Engineering, School of Materials Science and Engineering, South China University of Technology, Guangzhou, 510641, PR China
[b] National Engineering Research Center for Tissue Restoration and Reconstruction, PR China
[c] Key Laboratory of Biomedical Materials and Engineering, Ministry of Education, South China University of Technology, Guangzhou, 510006, PR China
[d] Department of Mechanical Engineering, University of Washington, Seattle, 98195, Washington, United States
[e] Guangzhou Regenerative Medicine and Health Guangdong Laboratory, 510005, PR China

ARTICLE INFO

Keywords:
Vitronectin
Protein adsorption
Surface chemistry
Cell adhesion
Molecular dynamics simulation

ABSTRACT

Biomaterial surface chemistry engenders profound consequences on cell adhesion and the ultimate tissue response by adsorbing proteins from extracellular matrix, where vitronectin (Vn) is involved as one of the crucial mediator proteins. Deciphering the adsorption behaviors of Vn in molecular scale provides a useful account of how to design biomaterial surfaces. But the details of structural dynamics and consequential biological effect remain elusive. Herein, both experimental and computational approaches were applied to delineate the conformational and orientational evolution of Vn during adsorption onto self-assembled monolayers (SAMs) terminating with -COOH, $-NH_2$, $-CH_3$ and -OH. To unravel the interplay between cell binding and the charge and wettability of material surface, somatomedin-B (SMB) domain of Vn holding the RGD cell-binding motif was employed in molecular dynamics (MD) simulations, with orientation initialized by Monte Carlo (MC) method. Experimental evidences including protein adsorption, cell adhesion and integrin gene expressions were thoroughly investigated. The adsorption of Vn on different surface chemistries showed very complex profiles. Cell adhesion was enabled on all Vn-adsorbed surfaces but with distinct mechanisms mostly determined by conformational change induced reorientation. Higher amount of Vn was observed on negatively charged surface (COOH) and hydrophobic surface (CH_3). However, advantageous orientations defined by RGD loop conditions were only obtained on the charged surfaces (COOH and NH_2). Specifically, COOH surface straightened up the Vn molecules and accumulated them into a higher density, whereas CH_3 surface squashed Vn and stacked them into higher density multilayer by tracking adsorption but with the RGD loops restrained. These findings may have a broad implication on the understanding of Vn functionality and would help develop new strategies for designing advanced biomaterials.

1. Introduction

Cell adhesion capability of implanted biomaterials is critical to the subsequent cell behavior and ultimate tissue response [1,2]. During the integration with host tissue, the surface physicochemical properties of implants determine cell affinity by adjusting the orientation, conformation and amount of adsorbed proteins from extracellular matrix (ECM) [3–6]. Adsorbed ECM proteins in specific state for cell attachment can work as pilots to guide cell adhesion [7]. Although the surface chemistry of biomaterials has been understood to play an elemental role in mediating the complex interplay at biomaterial-protein interface, it is still challenging to directly monitor the dynamic details of protein structure during adsorption process.

Vitronectin (Vn) is one of the important multi-functional ECM proteins in plasma. It was dedicated to various biological activities especially angiogenesis, plasminogen activation and cell adhesion [8]. The N-terminal domain (~44–53 residues) of Vn holds a 44 residues segment identical to somatomedin B (SMB), referred to as the SMB

Peer review under responsibility of KeAi Communications Co., Ltd.
* Corresponding author. Department of Biomedical Engineering, School of Materials Science and Engineering, South China University of Technology, Guangzhou, 510641, PR China.
** Corresponding author. Department of Biomedical Engineering, School of Materials Science and Engineering, South China University of Technology, Guangzhou, 510641, PR China.
E-mail addresses: duchang@scut.edu.cn (C. Du), imwangyj@163.com (Y. Wang).

https://doi.org/10.1016/j.bioactmat.2020.06.021
Received 17 April 2020; Received in revised form 26 June 2020; Accepted 27 June 2020

domain [9]. The SMB domain is crucial to wound healing via the binding to urokinase receptor (uPAR) and plasminogen activator inhibitor 1 (PAI-1) [10]. Notably, this domain hosts a key cell-binding site, the Arg-Gly-Asp (RGD) motif, thus is commonly regarded as the core functional segment of Vn [8]. The accessibility of these RGD motifs decides cell adhesion to Vn matrix by engaging and activating the integrin receptors on cell membrane like $\alpha_v\beta_1$, $\alpha_v\beta_3$ [11] and $\alpha_v\beta_5$ [12]. High-resolution crystal structure of SMB domain had been resolved [9]. Due to the similar cell-binding capability to full-length Vn [13], the SMB domain can serve as a decent representative for Vn to collect structural information and interpret cell-binding capacity during adsorption.

Although several studies have been carried out to examine the bioactivity of adsorbed Vn regulated by the electric property [14] or hydrophilicity [15,16] of material surfaces, hardly any detailed structural information or dynamics mechanism was elucidated. In a study by Bernards et al. [14], both negatively and positively charged substrates presented excellent cell-binding ability of adsorbed Vn. They inferred the importance of conformation to bioactivity of Vn when adsorbed on charged surfaces from denaturing experiment of Vn under acidic conditions. In addition, the inhibition by hydrophilicity of substrates on the bioactivity of Vn layer was observed by the use of mixed fibronectin and Vn [15]. Hydrophilicity of the substrate may decrease the Vn adsorption monotonically, as well as the bioactivity of adsorbed Vn due to fewer focal adhesions (FAs) [16]. However, direct evidence for detailed dynamic mechanism was still absent. The specific interplay and underlying mechanism of Vn adsorption under specific surface chemistry requires to be clearly clarified.

Herein, self-assembled monolayers (SAMs) with four kinds of terminal groups (-COOH, -NH_2, -CH_3 and -OH), served as model surfaces with opposite properties of charge or hydrophobicity, were well-prepared. The amount, orientation and morphologies of adsorbed Vn on the model surfaces were then investigated. Furthermore, the dynamic orientation and conformation of SMB domain segment and substrate-protein interactions during adsorption were studied by molecular dynamics (MD) simulation at atomic scale, following an initialization for the orientation configuration of protein by Monte Carlo method (MC). Finally, the adhesion and spreading of human mesenchymal stem cells (hMSCs) on Vn-adsorbed SAMs substrates were evaluated by observing cytoskeleton organization, focal adhesions formation and gene expression of related integrins. Based on the results, the adsorption dynamics and ultimate biological response of Vn were summarized and expected to provide an insight into understanding Vn functionality and surface modification for implanted biomaterials.

2. Materials and methods

2.1. SAMs preparation

Four 1 mmol·L^{-1} alkanethiol ethanol solutions were well-prepared in advance, specifically 11-mercaptoundecanoic acid (COOH, HS$(CH_2)_{10}$COOH), 11-amino-1-undecanethiol hydrochloride (NH_2, HS$(CH_2)_{11}NH_2$·HCl), 1-dodecanethiol (CH_3, HS$(CH_2)_{11}CH_3$), and 11-mercapto-1-undecanol (OH, HS$(CH_2)_{11}$OH). The gold slides were cleaned by a nitrogen plasma treatment previously and immersed in the 1 mmol·L^{-1} alkanethiol ethanol solutions overnight. The SAMs-modified substrates were rinsed with ethanol and then dried with a stream of nitrogen gas. The surface wettability and potential were detected by a contact angle meter (DSA25, Kruss, Germany) (n = 5) and the scanning Kelvin probe microscopy (SKPM) on an atomic force microscope (AFM, MFP-3D) (n = 4) with the use of PPP-EFM probes in air respectively.

2.2. Vn adsorption

SAMs substrates were immersed in 0.1 and 10.0 μg·mL^{-1} vitronectin (Vn, R&D Systems, USA) solutions and incubated for 1 h under 37 °C, 5% CO_2. The elemental compositions of bare and Vn-adsorbed SAMs samples with initial concentration of 10.0 μg·mL^{-1} were investigated by X-ray photoelectron spectroscopy (XPS, Escalab 250Xi, Thermo, USA). The morphology and surface potential distribution of Vn-adsorbed SAMs samples were detected and visualized by SKPM on an atomic force microscope (AFM, MFP-3D) with the use of PPP-EFM probes in the air.

Adsorption amounts and kinetics of vitronectin were studied by surface plasmon resonance assay (SPR, Plexera Kx5 V2, Plexera® Bioscience LLC, USA) with continuously inflowing Vn solutions of 1, 5, 10 and 20 μg·mL^{-1} over SAMs-modified SPR sensor surfaces at a rate of 2 μL·s^{-1}. The baseline was determined by inflowing protein-free PBS buffer. The adsorption and desorption of Vn were recorded and represented by the refractive unit (RU, 1 ng·mm^{-2}).

The functional capability of Vn adsorbed on SAMs was investigated by human vitronectin enzyme-linked immunosorbent assay kit (EHVTN, Thermo scientific, USA) by the use of monoclonal antibodies specifically binding to the epitopes of the RGD-holding domains (somatomedin-B domains) according to the manufacturer's instructions (n = 3).

2.3. SMB domain and SAMs models for simulations

As the representative for Vn, N-terminal somatomedin-B domain (SMB) of mature human plasma Vn all-atom structure was retrieved from RCSB protein data bank (PDB: 1S4G [9], model 20) with a net charge of −3. SMB domain has four disulfide pairs stabilizing its steric structure. A disulfide pair Cys25-Cys39 defines a cystine-stabilized α-helix (CSH motifs) within a fairly large loop (Fig. S1). SMB domain holds an RGD tripeptide comprising residues 45–47 within the C-terminal part. The angle between normal vector and the electric dipole moment of SMB molecule was denoted as the orientation angle (θ).

COOH-SAMs, NH_2-SAMs, CH_3-SAMs, and OH-SAMs model surfaces were constructed by adopting the $(\sqrt{3} \times \sqrt{3})R30°$ structure on Au(111) with HS$(CH_2)_{11}$COOH, HS$(CH_2)_{11}NH_2$, HS$(CH_2)_{11}CH_3$, and HS$(CH_2)_{11}$OH, respectively. The dimension of model surfaces was 5.196 × 5.500 nm^2. Ten terminal groups each were protonated and deprotonated randomly for COOH-SAMs and NH_2-SAMs respectively to adjust the surface charge density to 0.05 C·m^{-2}. The parameters of SAMs molecules were derived from the CHARMM36 force field [17].

2.4. Monte Carlo preoptimization

MC preoptimization was conducted prior to MD simulation to optimize the initial orientations. Systems were separated into three groups according to the charge of SAMs: negatively charged (COOH), positively charged (NH_2) and non-charged (CH_3 and OH). SAMs surfaces were simplified into endless planes with corresponding charge in the calculation, whereas SMB was simplified into a coarse-grained model referring to α-carbons. Electrostatic interaction and van der Waals interaction were calculated by using empirical equations and corresponding parameters from Zhou's work [18,19].

Coarse-grained SMB molecules were kept rigid throughout the calculation. The temperature of the system was set as 300 K. SMB molecules were placed over the endless plane by 10 nm. 80,000,000 MC circulations had been carried out in total by transferring and rotating SMB molecule around the center of mass. The first half of the MC calculation was performed for equilibration, whereas the rest half was for statistical analysis.

Optimized orientations from MC circulations were denoted as O_1, O_2, O_3, and O_4 accordingly (Fig. S5). The O_1 and O_2 orientations were applied as initial orientations for the MD simulations of COOH-SAMs and NH_2-SAMs systems respectively, whereas the O_2, O_3, and O_4 orientations were applied as initial orientations for the MD simulations of CH_3-SAMs and OH-SAMs systems.

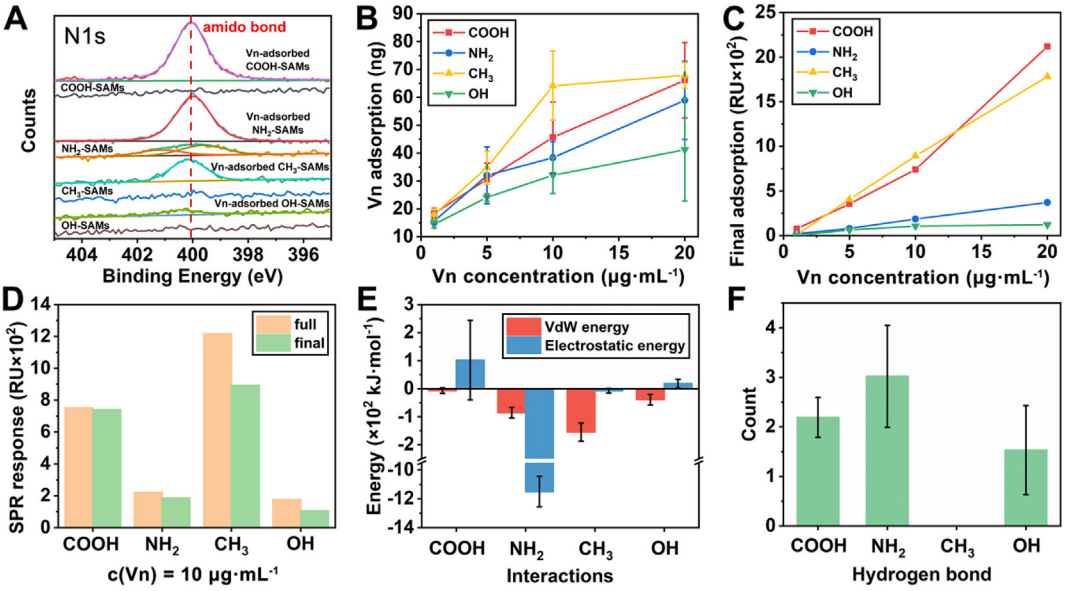

Fig. 1. Affinity of adsorbed Vn on SAMs. (A) XPS N1s spectrum of bare SAMs and Vn-adsorbed SAMs incubated with Vn solution of 10 μg·mL^{-1}. (B) Amount of adsorbed Vn measured by ELISA. (n = 3) (C) Final amount of adsorbed Vn measured by SPR. (D) SPR response of Vn-fully-adsorbed and Vn-finally-adsorbed SAMs when uploaded with 10 μg·mL^{-1} Vn solution. (E) Molecular mechanical interactions and (F) hydrogen bonds formed at the interface between SMB molecules and SAMs surfaces during the last 10 ns of MD simulations.

2.5. MD simulation

All-atom molecules of SMB were placed above SAMs surfaces by 0.5 nm in a simulation box of 5.196 × 5.500 × 8 nm^3. TIP3P model [20] was used to describe the water molecule for solvation. After filling up the box, water molecules were partly substituted by chlorine and sodium ions to neutralize the charge of entire systems. All the sulfur atoms in the sulfhydryl groups of SAMs molecules were kept fixed during the MD simulation.

MD simulations were carried out in a canonical ensemble with a time step of 2 fs. A Nosé-Hoover thermostat [21] was used to keep system temperature at 300 K. A Maxwell-Boltzmann distribution under 300 K allocated the initial velocity of each atom. Nonbonded interactions were calculated by a switched potential with a switch function starting at 9 Å and ending in zero at 10 Å, whereas the electrostatic interactions were calculated by the particle mesh Ewald method in 3dc geometry [22] with a cutoff distance of 12 Å. Hydrogen bonds were constrained by the LINCS algorithm [23]. Periodic boundary conditions were used in the *x* and *y* directions only. Two hard walls were used as implemented in the GROMACS-5.1.2 package [24]. All the parameters were derived from CHARMM36 force field [17].

Before production, the systems were relaxed through energy minimization to eliminate steric clashes and inappropriate geometry. Thereafter, a 100 ps NVT equilibration with position restraint on heavy atoms of SMB molecules was conducted to equilibrate the solvent and ions around protein. Finally, a 100 ns production MD simulation was carried out for each system. All the structures were visualized by VMD 1.9.2 [25] and PyMOL 2.2.0 [26]. Surface potential was calculated and visualized by APBS-PDB2PQR tools [27]. SMB-SAMs interfacial binding energies during the final stage were calculated by g_mmpbsa tools [28,29]. Secondary structure of SMB molecules was calculated by dssp package [30,31]. The root-mean-square deviation (rmsd) of the protein backbone, gyrate radius and electric dipole moment of SMB molecules were all calculated by GROMACS 5.1.2 package [24]. Judging from the settled features in most of the rmsd curves for Vn backbone, the last 10 ns of MD simulation was denoted as the final stage of adsorption for further statistical analysis.

2.6. Cell culture and cell adhesion assays

Human bone-marrow-derived mesenchymal stem cells (hMSCs) (Huxma-01001, Cyagen Biosciences Inc., USA) were cultured in growth medium (Huxma-90011, Cyagen Biosciences Inc., USA) (hMSCs basal medium mixed with 10% hMSCs-qualified fetal bovine serum, 1% penicillin-streptomycin and 1% glutamine). 10 × 10 mm^2 Vn-adsorbed SAMs were pre-blocked with 3% BSA solution under a humidified condition of 37 °C, 5% CO_2 prior to cell seeding. Early passage cells (≤6) were seeded on samples at a density of 1 × 10^4 cells·cm^{-2} and cultured for 12 h.

Cytomorphology study. After fixed and permeabilized, the hMSCs samples were incubated in the 1:100 diluted anti-vinculin antibody Alexa Fluor®647 (red) (ab196579, Abcam, USA) at 4 °C for 12 h for the immunostaining of focal adhesions. Afterward, the F-actin and nuclei of the cells were stained with Alexa Fluor®488 (green) (ThermoFisher Scientific, USA) for 20 min and DAPI (blue) (Beyitime, China) for 5 min respectively. The cytomorphology was observed by confocal laser scanning microscopy (CLSM, TCS SP8, Leica, Germany) (n = 2).

Evaluation of integrin gene expression. Total RNA was isolated by Hipure Total RNA Kits (Magentec, China) and reverse transcribed into cDNA using PrimeScript® RT reagent Kit with gDNA Eraser (TaKaRa Biotechnology, Japan) according to the manufacturer's protocol (n = 4). RT-PCR reactions were carried out with the SYBR Green System (Invitrogen, USA). Samples were held at 95 °C for 10 min, followed by 40 cycles at 95 °C for 15 s and 60 °C for 1 min. The relative quantification of target genes was processed by the $2^{-\Delta\Delta Ct}$ method (n = 4) using the primer and probe sequences (TaKaRa Biotechnology, Japan) as listed in Table S1.

3. Results

3.1. Adsorption affinity of Vn

In the XPS N1s spectra (Fig. 1A), the height of peaks at 400.2 eV representing the amide nitrogen [32] are positively related to the amount of Vn. The highest peak for Vn adsorption among all groups was observed at the negatively charged surface (COOH-SAMs), whereas the least was found at the non-charged hydrophilic surface (OH-SAMs).

Interestingly, Vn has a net negative charge at physiological conditions [33] like SMB domain, which was supposed to be rejected from COOH-SAMs (Fig. 1E). It seems odd to have a higher Vn adsorption on like-charged COOH-SAMs than opposite-charged NH_2-SAMs (Fig. 1A–D). In view of the high flexibility of Vn structure [14], possible intrinsic changes may take place in the adsorption and affect the efficiency of adsorption. Without driving forces like electrostatic interactions, hydrophobic interaction plays a vital role in driving the adsorption of Vn on the non-charged hydrophobic surface (CH_3-SAMs).

Adsorption from Vn solutions with different concentrations were further quantified by Vn-ELISA and SPR assay (Fig. 1B–D). Vn-ELISA assay measures the amount of active RGD sites rather than adsorbed Vn, whereas SPR assay measures the total amount of adsorbed Vn. The binding conditions of Vn could be roughly inferred from the differences between two results.

SPR assay shared a similar amount relationship with Vn-ELISA test at 10 $\mu g{\cdot}mL^{-1}$ (Fig. 1C&D). The smaller gap between COOH-SAMs and NH_2-SAMs in ELISA curves implied possible conformational change may took place in the SMB domain to deactivate the binding of detecting antibody. The highest Vn adsorption was observed on CH_3-SAMs and reached a "saturated" state at 10 $\mu g{\cdot}mL^{-1}$. The higher adsorption on CH_3-SAMs at 20 $\mu g{\cdot}mL^{-1}$ in SPR assay may suggested a fully adsorbed Vn monolayer at 10 $\mu g{\cdot}mL^{-1}$. As indicated in the binding energies calculated from the MD simulations, strong vdW interactions, i.e. mostly the hydrophobic interactions, dominantly stabilized the adsorbed SMB on CH_3-SAMs. Hydrophobic interaction is known to be entropically induced in the presence of water molecules. Lacking polar interaction formed at the interface (Fig. 1F), the adsorbed SMB is free to slide on CH_3-SAMs. The sliding may help eliminating the space between adsorbed proteins and thus increase the adsorption density.

Apart from amount, kinetics in the adsorption and desorption of Vn was also studied by fitting the association and dissociation phases from SPR assay (Fig. S4). Corresponding kinetic rate constants were calculated as listed in Table 1. The highest K_{off} on CH_3-SAMs among all groups manifested the fragile interactions of a large portion of adsorbed Vn with the substrate. We postulate that the interaction between later adsorbed Vn and substrate was cut down by the previous adsorbed Vn layers. Surprisingly, the lowest K_D was obtained for the COOH-SAMs, suggesting a considerable efficiency of Vn on negatively charged surfaces (Fig. 2D). This unexpected high efficiency on COOH-SAMs suggested a vital role of the impingement on the protein properties by material surfaces in Vn adsorption.

In particular, the highest K_{on} was obtained for OH-SAMs, suggesting the adsorption was promoted possibly due to local charge and weak resistance. Weak interaction of non-charged hydrophilic surfaces (Fig. 1E) confirmed the behavior of Vn involves repeated adsorption and desorption as shown in the trajectories from MD simulations (see supporting materials).

3.2. Morphologies of adsorbed Vn

0.1 $\mu g{\cdot}mL^{-1}$ (low concentration) and 10.0 $\mu g{\cdot}mL^{-1}$ (high concentration) Vn solutions were employed in the incubation to further investigate the morphology of adsorbed Vn on SAMs-modified surfaces (Fig. 2A). In light of monitoring the structural details directly, representative structures of adsorbed SMB in the final stage were visualized (Fig. 2B).

Vn layer covered the COOH-SAMs surface with a higher density at 10.0 $\mu g{\cdot}mL^{-1}$, which was similar to the case of NH_2-SAMs. When incubated at a lower concentration as 0.1 $\mu g{\cdot}mL^{-1}$, scattered Vn granules were observed on both substrates. Differently, the scattered Vn multimers demonstrated uniform mountain-like shape orienting to a similar direction on COOH-SAMs. Combine the results from MD simulation, SMB was unfolded with an "End-on" orientation on COOH-SAMs during the final adsorption stage (Fig. 2B). RGD loop was unrestrained and accessible for cell binding. At 60 ns of the simulation, SMB first anchored to the COOH-SAMs surface by two N-terminal basic residues (Lys6 and Arg8), and then unfolded into uniform shape during the post-anchoring period, which may explain the uniform mountain-like morphology of Vn. In contrast, SMB was slightly squashed but well-folded with a "Back-on" orientation on the NH_2-SAMs where RGD loop was unrestrained. The α-helix (Glu23-Gln29) in the origin structure was destroyed due to the binding of acidic residues (Asp22 and Glu23) with substrate.

On hydrophobic CH_3-SAMs, adsorbed Vn were aligned adjacently to form a branch shape at 0.1 $\mu g{\cdot}mL^{-1}$. Substrate surfaces and previous adsorbed Vn may play a big part in drawing the newly adsorbed Vn closer by interacting with them simultaneously. Particularly, the fluctuation in the height of Vn layer suggested an unfolded structure. The unfolding was further confirmed in all MD simulations for CH_3-SAMs. SMB was adsorbed on the CH_3-SAMs with a similar "Side-on" orientation regardless of the initial configure (Fig. 2B). RGD loops were restrained by substrates and deactivated for integrin binding. With higher concentration, unfolded Vn mutually crowded to form multilayers averagely covering substrate with an even higher amount compared to charged substrates. The upper Vn layer seemed to be incomplete probably due to the cutting down of hydrophobic interaction by the subjacent Vn layer.

Adsorbed Vn on hydrophilic OH-SAMs demonstrated scattered granule-like morphology but with a larger size at 10.0 $\mu g{\cdot}mL^{-1}$ than that at 0.1 $\mu g{\cdot}mL^{-1}$. The polar -OH groups of OH-SAMs surfaces tend to form hydrogen bonds with adjacent water molecules and make for a water layer coating. In sight of the weak interaction implied in MD simulation (Fig. 1E), adsorbed water molecules on hydrophilic surfaces may physically block direct binding of Vn to the substrate, as observed in the simulation results (Fig. S7). Thereafter, Vn was preferably adsorbed onto the earlier adsorbed Vn, forming larger aggregates. As indicated in the results of simulations, RGD loops were restrained to the substrate in O_3-OH and O_4-OH. "Side-on" pattern in O_2-OH was similar to that in O_4-OH, where the RGD was likely to interact with substrate and develop into a deactivate state, as displayed in the movies (see supporting materials).

Table 1
Kinetic rate constants of the adsorption and desorption of Vn on SAMs-modified substrates.

SAMs	Average association rate constant (K_{on}) ($M^{-1}s^{-1}$)	Average dissociation rate constant (K_{off}) (s^{-1})	Equilibrium dissociation constant (K_D) (M)
COOH	2.77×10^3	3.62×10^{-8}	1.31×10^{-11}
NH_2	1.39×10^4	1.11×10^{-4}	7.96×10^{-9}
CH_3	6.09×10^3	3.09×10^{-4}	5.08×10^{-8}
OH	2.83×10^4	2.67×10^{-4}	9.43×10^{-9}

3.3. Binding patterns of SMB domain

The contribution of residual binding energies indicated a more exact binding poses of SMB (Fig. 3). Adsorption on COOH-SAMs was contributed mostly by the molecular polarity of SMB molecule. Two N-terminal basic residues (Lys6 and Arg8) served as binding sites to support the anchoring of SMB. On the contrary, the adsorption was stabilized by two acidic residues (Asp22 and Glu23) at the N-terminal end of α-helix on NH_2-SAMs surface. Notably, barely any contributions at the C-terminal part indicated non-binding RGD loops in both charged systems. However, C-terminal part of SMB bore strong contact with all non-charged surfaces. The restrained state of RGD loops is likely to harm the cell-binding capability of SMB. Flattened SMB molecule with a meta-stable structure was observed on all hydrophobic surfaces (Fig. 2B). The high contribution of both central and C-terminal part of the hydrophobic core confirmed the unfolding of SMB. In contrast, SMB was likely to be adsorbed with a restrained RGD loop on OH-SAMs in

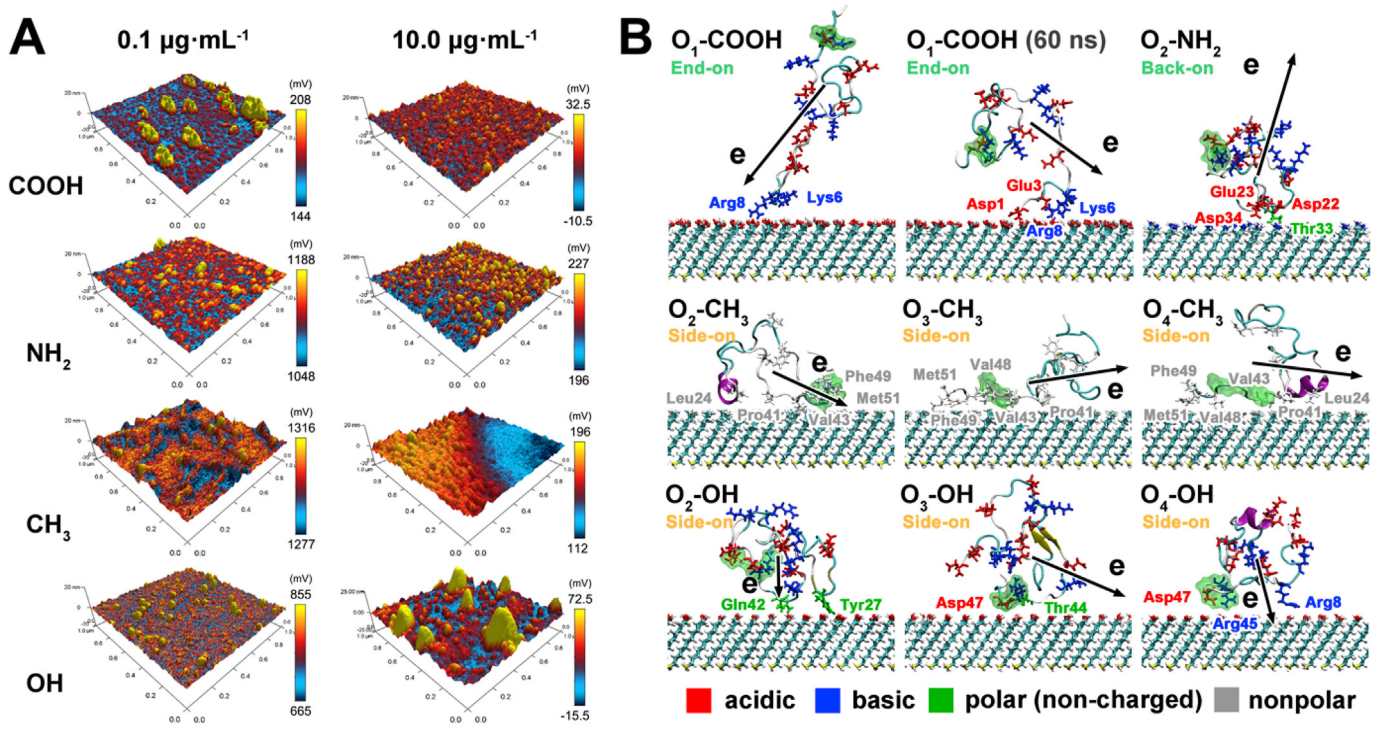

Fig. 2. (A) Surface potential profile of Vn-adsorbed SAMs incubated with 0.1 μg·mL^{-1} and 10.0 μg·mL^{-1} Vn solutions. 3D photos of Vn-adsorbed SAMs were constructed from height data and recolored according to nap potential data. (B) The final visualization state of SMB-adsorbed systems. The state of O_1-COOH system at 60 ns is showed additionally to visualize the pre-unfolding structure. RGD loops on SMB are presented in transparent green Surf mode.

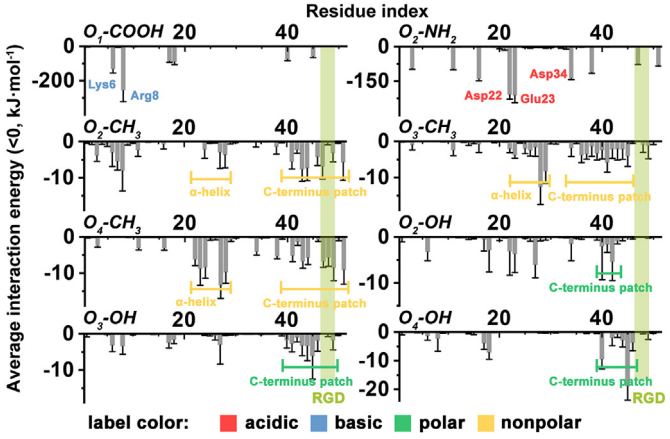

Fig. 3. Contributions of each residue of SMB to the binding interactions with SAMs surfaces. The residues or parts that made high contributions are labeled.

the final stage, but repeated reorientation could hardly define a preferable binding state of SMB.

3.4. Conformational evolutions of SMB domain

The structure of Vn may undergo severe deformation under intense conditions [34], so as SMB. Notably, bursts in the curves of both rmsd and gyrate radius were observed in O_1-COOH starting from 70 ns and lasting for about 20 ns (Fig. 4A&B), indicating drastic change in the structure of SMB. Although the structural change in the early period seemed to be restored from 55 ns, the structure of adsorbed SMB was somehow altered significantly afterward. RGD loop was decomposed into coils occasionally in all systems (Fig. 4C), increasing the flexibility of itself. The bioactivity was expected to be slightly improved with these more flexible RGD loops.

The conformational change of SMB molecule in O_1-COOH indicated a three-stage adsorption: approaching, anchoring and unfolding. The α-helix was first destroyed during approaching and reconstructed after anchoring on the substrate due to no restraints at the central part (Fig. 4C). Thereafter, continuous strong repulsive forces broke the α-helix into shorter helices or even loops, and unfolded SMB eventually.

For O_2-CH_3 and O_4-CH_3, the α-helix (Glu23-Gln29) in origin structure was first destroyed and then reconstructed in the long term. Despite the fact that the aromatic ring of tyrosine is a non-polar group, the phenolic hydroxyl group somehow makes it more acidic. The hydrophobic tyrosine on α-helix (Tyr27 and Tyr28) interacted with the substrate and destroyed the α-helix, but the phenolic hydroxyl group released the part and supported the reconstruction afterward.

3.5. Cell adhesion on Vn-adsorbed SAMs

Adhered hMSCs were well-spread on all substrates, with pseudopods along the cell periphery (Fig. 5A). Higher spreading area of hMSCs was observed on Vn-adsorbed COOH-SAMs and NH_2-SAMs (Fig. S8). Higher aspect ratio of cells attached on CH_3-SAMs indicated a slenderer shape in the morphologies. Particularly, More vinculin-containing focal adhesions (FAs) on charged surfaces also implied a better cellular affinity [15], which seemed to result from the beneficial orientations of adsorbed Vn. Rarely any new FAs was observed at the leading edge of cells on CH_3-SAMs, possibly indicating the inhibition of cell migration and spreading [35].

We also investigated the gene expression of integrins at 12 h (Fig. 5B). All gene expression level of integrins on charged SAMs surfaces showed superiority compared to those on non-charged ones, which was consistent with morphology results. The up regulation of integrin genes manifested the fact that Vn matrix can trigger the intracellular signals with actin cytoskeleton and promote cell adhesion and spreading.

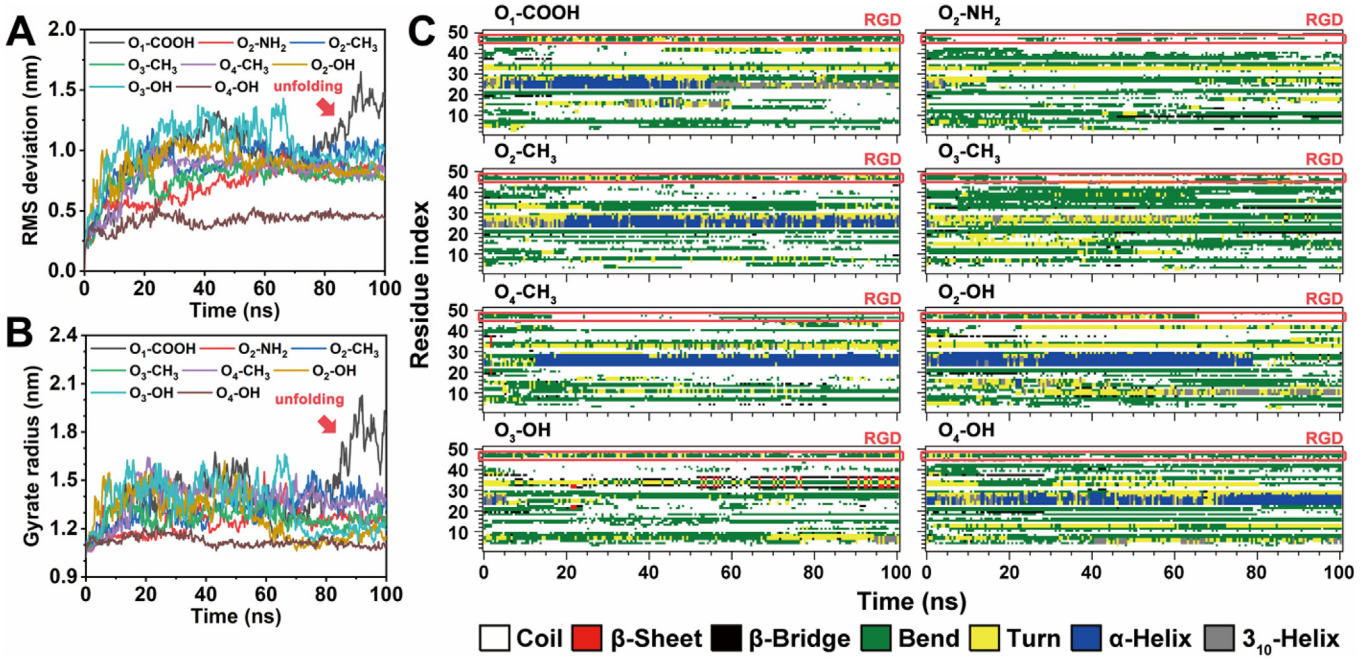

Fig. 4. (A) Rmsd of SMB backbone. (B) Gyrate radius of SMB molecules. (C) Secondary structure of SMB molecules during MD simulation. RGD loops are labeled out with red boxes.

4. Discussion

Biomaterial surface chemistry is known to play an essential role in mediating adsorption behavior of proteins and likely inducing variations in protein structure [5,14]. Properties of adsorbed proteins on the surface primarily determine the biocompatibility of implanted biomaterials [3]. With the developing of MD simulations, explicitly deciphering of the structural information and dynamic mechanism during protein adsorption becomes feasible.

Adsorption of Vn on different surface chemistries showed very complex profiles relating to amount, efficiency and rate. Results of XPS, SPR and ELISA (Fig. 1A–D) implied that Vn appeared to be preferably adsorbed on surfaces with higher hydrophobicity. Negatively charged surface seemed to be more favorable than positively charged for Vn though the protein itself is negatively charged. Indeed, our findings are consistent with other studies [14,36]. Dramatic changes in structure of SMB domain under acidic conditions indicated the structural flexibility of SMB domain [14]. The tertiary structure of SMB domain and flexible linkers between domains of Vn tended to be altered under continuous repulsive electrostatic force, as implied by the unfolded structure (Fig. 2B). This conformational change likely created the non-spherical but uniform shape of the adsorbed Vn multimers on COOH-SAMs (Fig. 2A), and also a compromised detection by ELISA comparing to that by XPS (Fig. 1A&B). The unfolding in structure reduces the recognizability for antibodies but straighten up the protein to a higher packing density on COOH-SAMs. On the non-charged hydrophobic surfaces (CH_3-SAMs), strong hydrophobic interactions unfolded the adsorbed Vn into a more disordered structure. The structural rearrangement may save space for later adsorption to reach a higher amount.

Based on the kinetic rate constants fitted and calculated from SPR assay (Table 1), association rate of Vn shared a different trend with dissociation rate. Although repulsive electrostatic interaction impeded a fast adsorption on COOH-SAMs, the unfolded structure of Vn enhanced adsorption capacity and reinforced the binding with substrate. On positively charged NH_2-SAMs, the attractive electrostatic

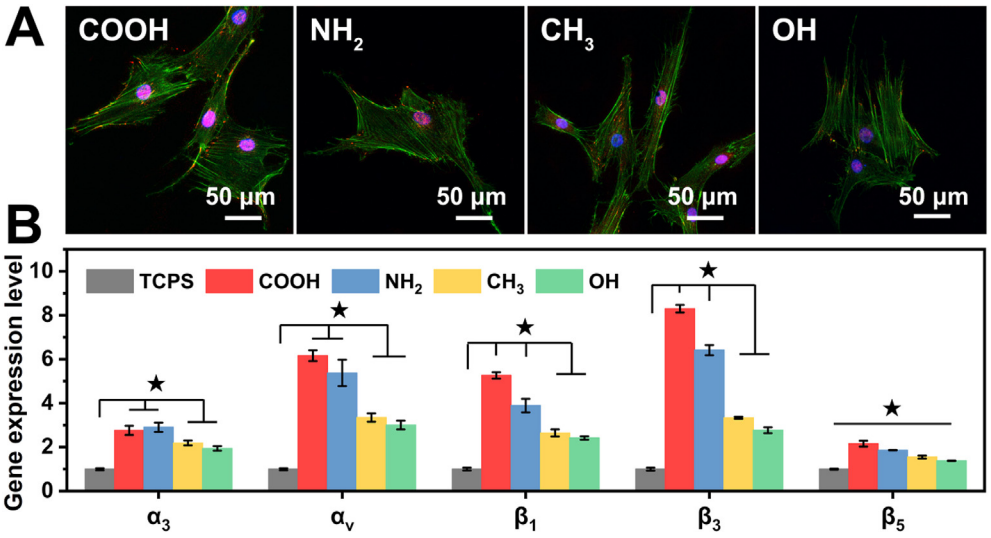

Fig. 5. (A) Morphology of adhered hMSCs on Vn-adsorbed SAMs after cultured for 12 h. The cytoskeleton (green) and nuclei (blue) of hMSCs were presented. Focal adhesions formation was examined through immunostaining of vinculin (red). (B) Gene expression of integrins associated with Vn. TCPS served as the blank. ★ denoted significant difference ($p < 0.05$).

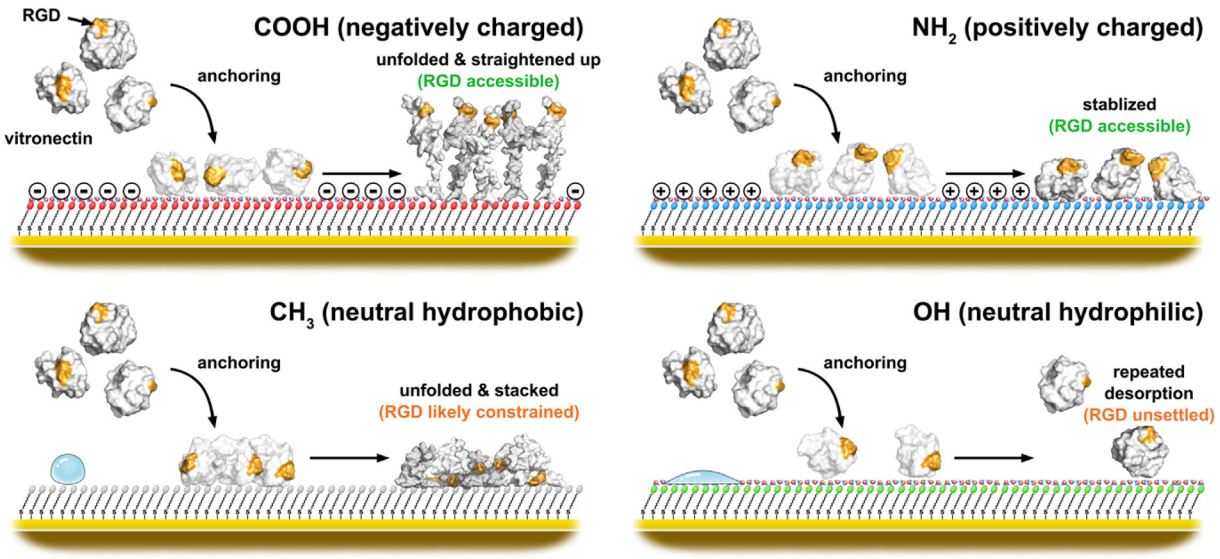

Fig. 6. Schematic diagram of underlying mechanisms for Vn adsorption. Vn was unfolded by continuous repulsive electrostatic interaction on negatively charged surfaces, improving the density of adsorption layer. Similarly, hydrophobic surfaces also unfolded Vn to bring the hydrophobic core from inside out and stacked them into multilayers. Orientation of Vn was stable on positively charged surfaces, but adsorbed Vn with low density was likely to reorient continuously on hydrophilic surfaces due to vulnerable interaction.

interaction appeared to adsorb Vn with a more stabilized structure. Dissociation rate of adsorbed Vn was generally higher on non-charged substrates due to the absence of electrostatic interaction. Particularly, non-charged hydrophilic OH-SAMs subjected to both high association rate and dissociation rate. After diffusion from the bulk solution, Vn anchors to the water-substrate interface via interaction of hydrophilic groups with the water adjacent to the hydrophilic OH-SAMs surfaces (Fig. S7). Anyhow, due to the heterogeneity from different residual properties, strong interactions of Vn with the other SAMs surfaces may pose a repulsive force on the Vn and lead to a flux in orientations before anchoring. Lacking these forces enhanced the association rate of Vn relatively on OH-SAMs surfaces compared to the others, but also failed to initiate the lockdown process, causing a high dissociation rate. Hence, the behavior of Vn on OH-SAMs involved repeated adsorption and desorption processes, making the orientation of Vn become uncertain. On hydrophobic CH_3-SAMs, the kinetics of Vn adsorption on CH_3-SAMs subjected to a tracking model [37], in which cooperative adsorption was proceeded due to the tracking of proteins to the binding sites close to pre-adsorbed proteins. Cooperative adsorption crowds adsorbed Vn into a much compact layer. However, the pre-adsorbed Vn layer on fully covered substrate altered the hydrophobicity of surface, leading to a weaker anchoring of subsequent adsorbed Vn. Internal rearrangement of protein structure is believed to make for a more effective lock-down process after anchoring [38]. The disordered structure of Vn may endow stronger ability to fill the fleeting voids of strongly bound water layer on the substrate to reach a more stable adsorption state ultimately on both COOH-SAMs and CH_3-SAMs.

Conformational-change-induced reorientation of adsorbed Vn defines the flexibility of RGD loops and decides cell response ultimately, though the adsorption amount is related to the amount of potential binding sites. MD simulations had depicted a clear picture on detailed structural and functional information of the key domain of Vn. RGD loops had higher flexibility in unfolded “End-on” orientation on COOH-SAMs or “Back-on” orientation on NH_2-SAMs, which were supposed to promote cell adhesion. The predictions were well-confirmed by the higher expression of integrin genes on charged substrates. In contrast, RGD loops were likely to be restrained on non-charged substrates, indicating no promotion to cell adhesion. Adhesion of hMSCs also proved the prediction by the fact that cell adhesion was relatively impeded on neutral substrates. Anyhow, weakly adsorbed Vn still has the chance to make for a beneficial orientation for RGD loops by rotation on hydrophilic substrates, but low coverage still limited the number of binding sites for integrins.

Human Vn exists as an intact ~75-kDa molecule, or as 65- and 10-kDa polypeptides linked by two disulfide bonds [39]. Preceded by a 19-residue signal peptide, a mature Vn consists of an N-terminal SMB domain (Asp1-Glu53), a central domain (Pro131-Pro342) holding a four-bladed β-propeller structure, and a C-terminal domain (Ala347-Leu459) engaging in the binding to heparin and collagen [40]. Prior studies have noted the sufficient integrin binding capability of SMB domain itself, but not as its full function in cell adhesion and spreading without the heparin-binding domain [13,41]. SMB domain can act as a qualified alternative for full-length Vn in the study of cell-binding capability in light of missing resolved crystal structure for the rest part. It suggested that the heparin binding site on C-terminal domain can selectively enhance osteoblast adhesion by specifically interacting with membrane glycosaminoglycans [42]. Several studies also indicated that the hemopexin domain signature of central and C-terminal domain enhanced the stiffness of Vn through multimerization, which allows formation of stronger binding to integrin and a well-organized actin cytoskeleton [13,40,43]. Notably, no dissociation of Vn after half cleavage of C-terminal heparin-binding domain indicated little or none appreciable contribution to conformational stability [44], which may imply the insignificance of C-terminal domain structure in dynamic evolution of Vn conformation. Anyhow, our study has systemically elucidated the mechanism details for the cell-binding core domain of Vn, but the structural changes and influence of the rest part still worth further investigation on the premise of resolved high-resolution crystal structure.

Collectively, the patterns are different for Vn adsorption on each substrate (Fig. 6). Charged substrates promoted cell adhesion due to the beneficial conditions of RGD loops. The unfolding dynamics of adsorbed Vn demonstrated distinctive effect of conformational changes on COOH-SAMs and CH_3-SAMs: COOH-SAMs imposed continuous electrostatic repulsive interaction on adsorbed Vn, and eventually unfolded the SMB domain into an RGD-flexible “End-on” orientation endowing Vn with better cell-binding capability. CH_3-SAMs unfolded adsorbed Vn by strong hydrophobic interaction, which is similar in the cases of other proteins [45]. Additionally, the weak interaction on OH-SAMs destabilized the attachment of Vn. Repeated adsorption and desorption had

led to the flux in the orientation of Vn, reducing the capability for cell adhesion eventually.

5. Conclusion

Dynamics and structural information of Vn during adsorption on model surfaces with opposite properties in charge or free energy were investigated by the adjoint use of experimental and computational methods. The cell-binding capability was predicted by the simulation and experimentally evaluated by the adhesion assessment of hMSCs.

Vn preferably adsorbed on negatively charged or hydrophobic surfaces, where its structure was likely to unfold. Negatively charged COOH-SAMs surface straightened up the Vn molecules and accumulated them forming a high-density protein layer, whereas non-charged hydrophobic CH_3-SAMs surface squashed the Vn molecules but still stacked them into a higher-density multilayer by tracking adsorption. In simulations results, the more beneficial orientations with unrestrained RGD loop on charged surfaces were predicted to promote cell adhesion, which was subsequently confirmed by hMSCs adhesion assay. Cell adhesion results demonstrated divergent extents of enabled hMSCs adhesion on all Vn-adsorbed surfaces. But the underlying mechanisms were different relating to the amount and highly depending on the conformational change induced reorientation of Vn. Our findings may shed light on the mediating mechanism of biomaterial surfaces on protein adsorption dynamics and the subsequent cell adhesion and expected to exert great value in understanding Vn functionality and designing advanced biomaterials.

Associated content

Supporting Information. Brief statement in non-sentence format listing the contents of the material and the movies of visualized adsorption process in all systems are supplied as Supporting Information.

Data availability

All data needed to evaluate the conclusions in the paper are present in the paper and/or the Supplementary Materials. Additional data related to this paper are available upon requests to the authors.

CRediT authorship contribution statement

Tianjie Li: Methodology, Software, Validation, Investigation, Data curation, Visualization, Writing - original draft. **Lijing Hao:** Conceptualization, Methodology, Writing - review & editing. **Jiangyu Li:** Resources, Methodology. **Chang Du:** Conceptualization, Writing - review & editing, Supervision. **Yingjun Wang:** Writing - review & editing, Supervision, Project administration.

Declaration of competing interest

The authors declare no competing financial interest.

Acknowledgement

This work was financially supported by the National Key R&D Program of China (2017YFC1105000), Science and Technology Planning Project of Guangdong Province (2017B030314008), National Natural Science Foundation of China (51572087, 31700823), Shenzhen Science and Technology Innovation Committee (JCYJ20170818160503855), Outstanding Scholar Program of Guangzhou Regenerative Medicine and Health Guangdong Laboratory (2018GZR110102001), GDST-NWO science industry cooperation programme Chemistry (2018A050501006), Natural Science Foundation of Guangdong Province of China (2020A1515011354), and the 111 Project (B13039).

Appendix A. Supplementary data

Supplementary data to this article can be found online at https://doi.org/10.1016/j.bioactmat.2020.06.021.

References

[1] X. Wang, F.A. Shah, F. Vazirisani, A. Johansson, A. Palmquist, O. Omar, K. Ekström, P. Thomsen, Exosomes influence the behavior of human mesenchymal stem cells on titanium surfaces, Biomaterials 230 (2020) 119571, , https://doi.org/10.1016/j.biomaterials.2019.119571.

[2] K. Li, Y. Xue, T. Yan, L. Zhang, Y. Han, Si substituted hydroxyapatite nanorods on Ti for percutaneous implants, Bioact. Mater. 5 (2020) 116–123, https://doi.org/10.1016/j.bioactmat.2020.01.001.

[3] M.N. Abdallah, S.D. Tran, G. Abughanam, M. Laurenti, D. Zuanazzi, M.A. Mezour, Y. Xiao, M. Cerruti, W.L. Siqueira, F. Tamimi, Biomaterial surface proteomic signature determines interaction with epithelial cells, Acta Biomater. 54 (2017) 150–163, https://doi.org/10.1016/j.actbio.2017.02.044.

[4] M.S. Lord, M. Foss, F. Besenbacher, Influence of nanoscale surface topography on protein adsorption and cellular response, Nano Today 5 (2010) 66–78, https://doi.org/10.1016/j.nantod.2010.01.001.

[5] P. Roach, D. Farrar, C.C. Perry, Interpretation of protein adsorption: surface-induced conformational changes, J. Am. Chem. Soc. 127 (2005) 8168–8173, https://doi.org/10.1021/ja042898o.

[6] F. Gao, Y. Hu, G. Li, S. Liu, L. Quan, Z. Yang, Y. Wei, C. Pan, Layer-by-layer deposition of bioactive layers on magnesium alloy stent materials to improve corrosion resistance and biocompatibility, Bioact. Mater. 5 (2020) 611–623, https://doi.org/10.1016/j.bioactmat.2020.04.016.

[7] E.A. Cavalcanti-Adam, Building nanobridges for cell adhesion, Nat. Mater. 18 (2019) 1272–1273, https://doi.org/10.1038/s41563-019-0537-7.

[8] V. De Lorenzi, G.M. Sarra Ferraris, J.B. Madsen, M. Lupia, P.A. Andreasen, N. Sidenius, Urokinase links plasminogen activation and cell adhesion by cleavage of the RGD motif in vitronectin, EMBO Rep. 17 (2016) 982–998, https://doi.org/10.15252/embr.201541681.

[9] A. Mayasundari, N.A. Whittemore, E.H. Serpersu, C.B. Peterson, The solution structure of the N-terminal domain of human vitronectin: proximal sites that regulate fibrinolysis and cell migration, J. Biol. Chem. 279 (2004) 29359–29366, https://doi.org/10.1074/jbc.M401279200.

[10] A. Zhou, Functional Structure of the Somatomedin B Domain of Vitronectin, Protein Science, vol. 16, a publication of the Protein Society, 2007, pp. 1502–1508, https://doi.org/10.1110/ps.072819107.

[11] M.M. Pradas, M.J. Vicent, Polymers in Regenerative Medicine: Biomedical Applications from Nano-To Macro-Structures, John Wiley &, 2014 Sons.

[12] D. Varun, G.R. Srinivasan, Y.H. Tsai, H.J. Kim, J. Cutts, F. Petty, R. Merkley, N. Stephanopoulos, D. Dolezalova, M. Marsala, D.A. Brafman, A robust vitronectin-derived peptide for the scalable long-term expansion and neuronal differentiation of human pluripotent stem cell (hPSC)-derived neural progenitor cells (hNPCs), Acta Biomater. 48 (2017) 120–130, https://doi.org/10.1016/j.actbio.2016.10.037.

[13] C.R. Chillakuri, C. Jones, H.J. Mardon, Heparin binding domain in vitronectin is required for oligomerization and thus enhances integrin mediated cell adhesion and spreading, FEBS Lett. 584 (2010) 3287–3291, https://doi.org/10.1016/j.febslet.2010.06.023.

[14] M.T. Bernards, S. Jiang, pH-induced conformation changes of adsorbed vitronectin maximize its bovine aortic endothelial cell binding ability, J. Biomed. Mater. Res. 87 (2008) 505–514, https://doi.org/10.1002/jbm.a.31778.

[15] C.C. Barrias, M.C. Martins, G. Almeida-Porada, M.A. Barbosa, P.L. Granja, The correlation between the adsorption of adhesive proteins and cell behaviour on hydroxyl-methyl mixed self-assembled monolayers, Biomaterials 30 (2009) 307–316, https://doi.org/10.1016/j.biomaterials.2008.09.048.

[16] G. Toromanov, C. Gonzalez-Garcia, G. Altankov, M. Salmeron-Sanchez, Vitronectin activity on polymer substrates with controlled -OH density, Polymer 51 (2010) 2329–2336, https://doi.org/10.1016/j.polymer.2010.03.041.

[17] A.D. MacKerell, D. Bashford, M. Bellott, R.L. Dunbrack, J.D. Evanseck, M.J. Field, S. Fischer, J. Gao, H. Guo, S. Ha, D. Joseph-McCarthy, L. Kuchnir, K. Kuczera, F.T.K. Lau, C. Mattos, S. Michnick, T. Ngo, D.T. Nguyen, B. Prodhom, W.E. Reiher, B. Roux, M. Schlenkrich, J.C. Smith, R. Stote, J. Straub, M. Watanabe, J. Wiórkiewicz-Kuczera, D. Yin, M. Karplus, All-atom empirical potential for molecular modeling and dynamics studies of proteins, J. Phys. Chem. B 102 (1998) 3586–3616, https://doi.org/10.1021/jp973084f.

[18] J. Zhou, S.F. Chen, S.Y. Jiang, Orientation of adsorbed antibodies on charged surfaces by computer simulation based on a united-residue model, Langmuir 19 (2003) 3472–3478, https://doi.org/10.1021/la026871z.

[19] J. Zhou, J. Zheng, S.Y. Jiang, Molecular simulation studies of the orientation and conformation of cytochrome c adsorbed on self-assembled monolayers, J. Phys. Chem. B 108 (2004) 17418–17424, https://doi.org/10.1021/jp038048x.

[20] W.L. Jorgensen, J. Chandrasekhar, J.D. Madura, R.W. Impey, M.L. Klein, Comparison of simple potential functions for simulating liquid water, J. Chem. Phys. 79 (1983) 926–935, https://doi.org/10.1063/1.445869.

[21] W.G. Hoover, Canonical dynamics: equilibrium phase-space distributions, Phys. Rev. A. Gen. Phys. 31 (1985) 1695–1697, https://doi.org/10.1103/PhysRevA.31.1695.

[22] I.C. Yeh, M.L. Berkowitz, Ewald summation for systems with slab geometry, J. Chem. Phys. 111 (1999) 3155–3162, https://doi.org/10.1063/1.479595.
[23] B. Hess, H. Bekker, H.J.C. Berendsen, J.G.E.M. Fraaije, LINCS: a linear constraint solver for molecular simulations, J. Comput. Chem. 18 (1997) 1463–1472, https://doi.org/10.1002/(Sici)1096-987x(199709)18:12<1463 Aid-Jcc4 > 3.3.Co;2-L.
[24] M. Abraham, D. van der Spoel, E. Lindahl, B. HessGROMACS Development Team, GROMACS User Manual, (2016) version 5.1.2.
[25] W. Humphrey, A. Dalke, K. Schulten, VMD: visual molecular dynamics, J. Mol. Graph. 14 (33-8) (1996) 27–28, https://doi.org/10.1016/0263-7855(96)00018-5.
[26] L.L.C. Schrodinger, The PyMOL Molecular Graphics System, (2015) Version 2.2.0.
[27] E. Jurrus, D. Engel, K. Star, K. Monson, J. Brandi, L.E. Felberg, D.H. Brookes, L. Wilson, J. Chen, K. Liles, M. Chun, P. Li, D.W. Gohara, T. Dolinsky, R. Konecny, D.R. Koes, J.E. Nielsen, T. Head-Gordon, W. Geng, R. Krasny, G.W. Wei, M.J. Holst, J.A. McCammon, N.A. Baker, Improvements to the APBS Biomolecular Solvation Software Suite, Protein Science vol. 27, a publication of the Protein Society, 2018, pp. 112–128, https://doi.org/10.1002/pro.3280.
[28] N.A. Baker, D. Sept, S. Joseph, M.J. Holst, J.A. McCammon, Electrostatics of nanosystems: application to microtubules and the ribosome, Proc. Natl. Acad. Sci. U. S. A 98 (2001) 10037–10041, https://doi.org/10.1073/pnas.181342398.
[29] R. Kumari, R. Kumar, C. Open, Source Drug Discovery, A. Lynn, g_mmpbsa–a GROMACS tool for high-throughput MM-PBSA calculations, J. Chem. Inf. Model. 54 (2014) 1951–1962, https://doi.org/10.1021/ci500020m.
[30] K. Wakamura, K. Hirokawa, K. Orita, Dictionary of protein secondary structure: pattern recognition of hydrogen-bonded and geometrical features, Biopolymers 22 (1983) 2577–2637, https://doi.org/10.1002/bip.360221211.
[31] R.P. Joosten, T.A. te Beek, E. Krieger, M.L. Hekkelman, R.W. Hooft, R. Schneider, C. Sander, G. Vriend, A series of PDB related databases for everyday needs, Nucleic Acids Res. 39 (2011) D411–D419, https://doi.org/10.1093/nar/gkq1105.
[32] N. Graf, E. Yegen, T. Gross, A. Lippitz, W. Weigel, S. Krakert, A. Terfort, W.E.S. Unger, XPS and NEXAFS studies of aliphatic and aromatic amine species on functionalized surfaces, Surf. Sci. 603 (2009) 2849–2860, https://doi.org/10.1016/j.susc.2009.07.029.
[33] K.T. Preissner, D. Seiffert, Role of vitronectin and its receptors in haemostasis and vascular remodeling, Thromb. Res. 89 (1998) 1–21, https://doi.org/10.1016/S0049-3848(97)00298-3.
[34] T.J. Webster, L.S. Schadler, R.W. Siegel, R. Bizios, Mechanisms of enhanced osteoblast adhesion on nanophase alumina involve vitronectin, Tissue Eng. 7 (2001) 291–301, https://doi.org/10.1089/10763270152044152.
[35] M.A. Partridge, E.E. Marcantonio, Initiation of attachment and generation of mature focal adhesions by integrin-containing filopodia in cell spreading, Mol. Biol. Cell 17 (2006) 4237–4248, https://doi.org/10.1091/mbc.e06-06-0496.
[36] M. Bale, L. Wohlfahrt, D. Mosher, B. Tomasini, R. Sutton, Identification of vitronectin as a major plasma protein adsorbed on polymer surfaces of different copolymer composition, Blood 74 (1989) 2698–2706, https://doi.org/10.1182/blood.v74.8.2698.2698.
[37] M. Rabe, D. Verdes, J. Zimmermann, S. Seeger, Surface organization and cooperativity during nonspecific protein adsorption events, J. Phys. Chem. B 112 (2008) 13971–13980, https://doi.org/10.1021/jp804532v.
[38] M.J. Penna, M. Mijajlovic, M.J. Biggs, Molecular-level understanding of protein adsorption at the interface between water and a strongly interacting uncharged solid surface, J. Am. Chem. Soc. 136 (2014) 5323–5331, https://doi.org/10.1021/ja411796e.
[39] K. Kubota, S. Katayama, M. Matsuda, M. Hayashi, Three types of vitronectin in human blood, Cell Struct. Funct. 13 (1988) 123–128, https://doi.org/10.1247/csf.13.123.
[40] D. Xu, K. Baburaj, C.B. Peterson, Y. Xu, Model for the three-dimensional structure of vitronectin: predictions for the multi-domain protein from threading and docking, Proteins 44 (2001) 312–320, https://doi.org/10.1002/prot.1096 https://search.crossref.org/?q=D.+Xu%2C+K.+Baburaj%2C+C.B.+Peterson%2C+Y.+Xu%2C+Model+for+the+three-dimensional+structure+of+vitronectin%3A+predictions+for+the+multi-domain+protein+from+threading+and+docking%2C+Proteins.+44+%282001%29+312-320.
[41] S. Bergmann, A. Lang, M. Rohde, V. Agarwal, C. Rennemeier, C. Grashoff, K.T. Preissner, S. Hammerschmidt, Integrin-linked kinase is required for vitronectin-mediated internalization of Streptococcus pneumoniae by host cells, J. Cell Sci. 122 (2009) 256–267, https://doi.org/10.1242/jcs.035600.
[42] A. Zamuner, P. Brun, M. Scorzeto, G. Sica, I. Castagliuolo, M. Dettin, Smart biomaterials: surfaces functionalized with proteolytically stable osteoblast-adhesive peptides, Bioact. Mater. 2 (2017) 121–130, https://doi.org/10.1016/j.bioactmat.2017.05.004.
[43] S. Kumar, Cellular mechanotransduction: stiffness does matter, Nat. Mater. 13 (2014) 918–920, https://doi.org/10.1038/nmat4094.
[44] K. Shin, B.C. Lechtenberg, L.M. Fujimoto, Y. Yao, S.S. Bartra, G.V. Plano, F.M. Marassi, Structure of human Vitronectin C-terminal domain and interaction with < em > Yersinia pestis < /em > outer membrane protein Ail, Sci. Adv. 5 (2019), https://doi.org/10.1126/sciadv.aax5068 eaax5068.
[45] M. Rabe, D. Verdes, S. Seeger, Surface-induced spreading phenomenon of protein clusters, Soft Matter 5 (2009) 1039–1047, https://doi.org/10.1039/b814053g.